Nanoscale

ROYAL SOCIETY OF CHEMISTRY

PAPER

View Article Online
View Journal

Cite this: DOI: 10.1039/d6nr01509c

Coupling interfacial chemistry and temperature for anisotropy-enhanced sidewall evolution in silicon dioxide wet etching

Jinmeng Shi,† Aixi Pan, *† Rebecca Mac, Md Fahim Al Fattah, Zbig Wasilewski and Dayan Ban*

Received 17th April 2026,
Accepted 24th May 2026

DOI: 10.1039/d6nr01509c

rsc.li/nanoscale

Silicon dioxide (SiO_2) microstructures are widely employed in photonic and microelectronic devices. However, achieving well-controlled device profiles typically relies on costly dry-etching tools and complex fabrication workflows. Wet etching of SiO_2 in hydrofluoric acid (HF), while attractive for its simplicity and scalability, is commonly regarded as inherently isotropic, limiting sidewall control. This work demonstrates that pronounced and continuously tunable anisotropy can be achieved using a buffered oxide etch (BOE)-based wet etching strategy. By systematically modulating etchant chemistry, surfactant-assisted interfacial transport, and etching temperature, anisotropic selectivity is engineered at a relatively high etch rate while maintaining smooth and uniform profiles, without relying on high-cost fabrication methods. In particular, reducing the etching temperature leads to a reduction in the sidewall angle of 33% and an increase in the vertical-to-lateral etch-rate ratio of 16%. These results establish BOE-based wet etching as a simple, scalable, and cost-effective approach for near-anisotropic SiO_2 microfabrication with improved profile fidelity.

I. Introduction

SiO_2 is a foundational material in precision optics and microfabrication owing to its broad optical transparency from the ultraviolet (UV) to the infrared,[1,2] low thermal expansion,[3] excellent thermal-shock resistance,[4,5] and outstanding chemical durability.[6,7] These properties underpin the widespread use in optical components and micro-electro-mechanical systems (MEMS), including diffraction gratings,[8,9] photodetectors,[10] metasurfaces,[11,12] and waveguide-based devices.[13] A prominent example is surface-relief gratings (SRGs) on glass substrates for augmented reality (AR) architectures,[14] where the grating geometry critically determines diffraction efficiency, angular bandwidth, and ultimately optical throughput and field-of-view. Beyond display technologies, integrated diffractive SiO_2 metasurfaces enable scalable optical computing and photonic artificial intelligence (AI)[11] by encoding computational weights into phase and amplitude profiles, allowing low-energy, massively parallel on-chip inference *via* free-space light propagation.[12]

A variety of well-established microfabrication techniques have been developed for patterning SiO_2. Ion-beam milling offers strong directionality, but is constrained by low selectivity,[15] redeposition,[16,17] and high equipment cost,[18] restricting scalability to large-area substrates.[19,20] Plasma-based dry etching, including reactive ion etching (RIE) and inductively coupled plasma reactive ion etching (ICP-RIE), enables anisotropic profile control by contrast, it frequently suffers from polymer residual contamination,[21–23] micro-trenching,[24] loading effect,[25] alongside elevated tool complexity and cost.[19] Moreover, the electrically insulating nature of SiO_2 promotes surface charging during plasma etching, which can induce profile distortions and etch non-uniformity, further complicating wafer-level manufacturing.[22]

Considering these limitations, HF-based wet etching of SiO_2 typically produces smoother sidewalls with minimal surface damage while requiring comparatively simple and low-cost equipment, rendering it inherently compatible with wafer-scale and high-throughput manufacturing.[19,26] Notably, Konstantinova *et al.* demonstrated that buffered HF-based etchants enable the fabrication of deep and multilevel SiO_2 microstructures with high etch rates and low surface roughness,[27] providing a viable alternative to dry etching for precision oxide microfabrication. However, HF-based wet etching of SiO_2 is widely regarded as inherently isotropic,[28,29] due to pronounced lateral undercutting,[24] which severely limits its applicability. Previous studies have primarily investigated individual parameters influencing SiO_2 wet etching, such as buffering to regulate fluoride availability[30] or temperature[31] to

---

Department of Electrical and Computer Engineering, Waterloo Institute for Nanotechnology, University of Waterloo, Waterloo, N2L 3G1, Canada.
E-mail: a22pan@uwaterloo.ca

† JS and AP contributed equally to this work.

modulate etch kinetics in isolation. A systematic, multi-parameter exploration within a unified wet-etching framework that enables controllable and enhanced anisotropy has remained scarce.

Here, this work directly addresses the long-standing perception of intrinsic isotropy in SiO_2 wet etching by demonstrating controllable directional anisotropic sidewall formation using a modified three-parameter modulated BOE-based strategy. Etching directional selectivity and profile quality are systematically tuned through the combined control of etchant chemistry, surfactant-mediated wetting behavior, and etching temperature. Etching performance is quantitatively evaluated using direction-resolved vertical and lateral etch rates, calculated vertical-to-lateral ratio, etch inclination angle (α), and surface roughness. By mapping a comprehensive process window, conditions are identified under which lateral etching is effectively suppressed while high vertical etch rates and minimal surface roughness are maintained. Under these optimized conditions, the etch angle α is reduced to 67% of its initial value, accompanied by a 15% increase in the vertical-to-lateral etch-rate ratio. This work demonstrated a simple and scalable route for near-anisotropic SiO_2 microfabrication, which is readily extendable to waveguides, surface-relief grating couplers, and other diffractive optical elements requiring engineered sidewall geometries.

II. Experiment

As illustrated in Fig. 1, the proposed fabrication process was performed on a 4-inch fused silica wafer. The wafer was sequentially rinsed with acetone, isopropanol (IPA), followed by an oxygen (O_2) plasma treatment with 20 W radio frequency (RF) power, 20 sccm O_2 gas flow, and 20 mTorr chamber pressure to remove organic residues. Hexamethyldisilane (HMDS) treatment is applied after cleaning, a silane-based adhesion promoter that reacts with surface hydroxyl groups to form a hydrophobic interfacial layer, thereby improving the adhesion between the photoresist and the chip surface.

A 3.0 μm-thick negative photoresist AZ nLOF 2035 was then spin-coated at 3000 rpm and soft-baked at 110 °C for 1 minute (Fig. 1b). Stripe patterns with varying line widths (10, 25, 50, and 75 μm) and circle patterns with multiple diameters (100, 200, and 300 μm) were defined using a mask-less photolithography (MLA, Heidelberg Instruments, Fig. 1c) and developed to form stripe- and circular shaped openings in the resist (Fig. 1d). Under all etching conditions investigated in this work, stripe widths below 10 μm were completely lost due to lateral undercutting, establishing 10 μm as the minimum reliable stripe dimension.

A 40 nm chromium (Cr) layer was then deposited by electron-beam evaporation to serve as a hard mask (Fig. 1e). Owing to the high selectivity of HF-based wet etching toward metal masks, Cr was selected as it produces more pronounced and controllable lateral under-etching compared with commonly used metals such as Au and Pt.[29] The overhang profile of the photoresist enabled a lift-off process, during which the resist and the overlying Cr were removed, yielding well-defined Cr stripe patterns on the wafer (Fig. 1f).

After patterning, the samples were subjected to HF-based wet etching, followed by removal of the hard mask using a commercial Cr etchant. The etch profile was systematically tuned by adjusting the etchant composition, introducing a surfactant (Triton X-100), and controlling the etching temperature. Five representative parameter sets were investigated and are summarized in Table 1. Optimal anisotropic selectivity was

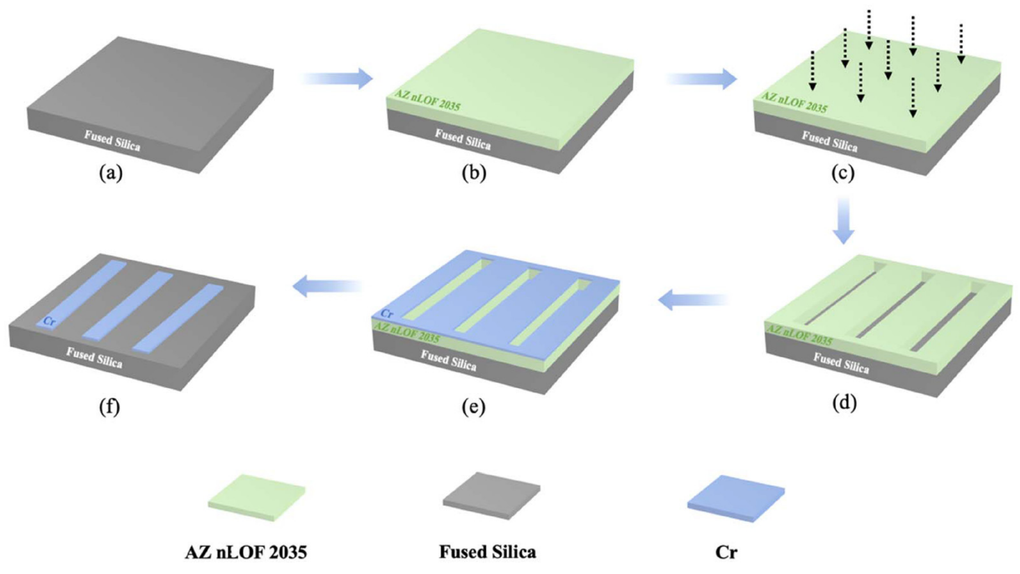

Fig. 1 Fabrication steps for wet-etched SiO_2 patterns. (a) A 4-inch fused silica chip after surface cleaning; (b) spin coat a layer of AZ nLOF 2035 negative photoresist; (c) photolithography; (d) development; (e) 40 nm Cr deposition; (f) lift-off process.

Table 1 HF-based wet etching conditions for the six samples

Sample number #	Etchant	HF : H_2O/ NH_4F	Temperature	Surfactant (Triton X-100)
1	Diluted HF	1 : 6	25 °C	—
2	BOE	1 : 6	25 °C	—
3	BOE	1 : 6	0 °C	—
4	BOE	1 : 6	25 °C	0.3 mL
5	BOE	1 : 6	0 °C	0.3 mL

achieved using an HF : NH_4F volume ratio of 1 : 6 with the addition of 0.3 mL Triton X-100 at 0 °C. Cross-sectional etch profiles were characterized by scanning electron microscopy (SEM, JEOL) after deposition of a thin iridium film, enabling both qualitative evaluation and quantitative analysis of etch anisotropy and morphological features.

III. Results and discussion

A. Role of etchant chemistry in HF and BOE systems

To compare BOE with diluted HF in deionized (DI) water for SiO_2 patterning, controlled comparative etching experiments were performed using an identical volumetric dilution ratio of 1 : 6 at 25 °C for 2 hours, as summarized in Table 1 (samples #1 and #2). This ratio is commonly employed in oxide wet etching and therefore represents a practically relevant processing condition.[32] Although the absolute fluoride activity differs between diluted HF and BOE at the same volumetric ratio, this comparison is intended to assess process robustness and pattern fidelity under commonly used etching conditions.

SiO_2 is etched by aqueous HF through proton (H^+)-assisted weakening of Si–O bonds ($HF \rightleftharpoons H^+ + F^-$), followed by nucleophilic attack by reactive fluoride species ($HF \rightleftharpoons H^+ + F^-$; $HF + F^- \rightleftharpoons HF_2^-$), ultimately forming soluble hexafluorosilicic acid ($SiO_2 + 6HF \rightleftharpoons H_2SiF_6 + 2H_2O$).[32] In unbuffered HF solutions, the strong coupling between surface reaction kinetics and local mass transport can lead to localized etch-rate amplification, whereby small initial surface irregularities promote sustained preferential etching and progressively evolve into etch pits. In contrast, BOE stabilizes the reactive fluoride species through equilibrium ($NH_4F + HF \rightleftharpoons NH_4^+ + HF_2^-$), thereby maintaining an effectively constant HF activity and suppressing the etch-rate decay commonly observed in unbuffered HF solutions.[30] As a result, BOE provides a more stable and reproducible etch environment.

Consistent with these chemical differences, distinct etch morphologies are observed, as shown in Fig. 2 sample #1 etched in diluted HF exhibits rough profiles with pronounced local undulations, a high density of etching pits, and severe over-etching near the mask-substrate interface. In contrast, BOE-etched sample #2 yields significantly smoother and more uniform profiles with continuous sidewalls and a sparse distribution of etching pits. These improvements are attributed to the buffered fluoride chemistry rather than thermal effects, as both processes were conducted under identical temperature conditions. Based on this qualitative morphological comparison, BOE was selected for subsequent quantitative parametric studies.

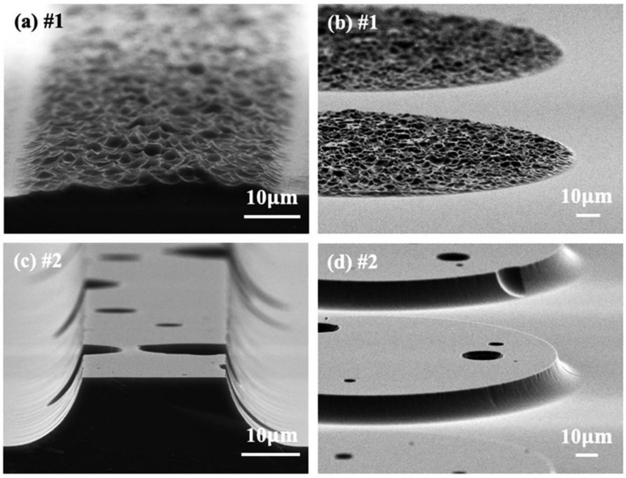

Fig. 2 SEM images of etch profiles in diluted HF and BOE under identical conditions (25 °C, 2 h). (a) Diluted HF (HF : H_2O = 1 : 6), 50 μm-wide stripes; (b) diluted HF (HF : H_2O = 1 : 6), 100 μm-radius circular features; (c) BOE (HF : NH_4F = 1 : 6), 50 μm-wide stripes; (d) BOE (HF : NH_4F = 1 : 6), 100 μm-radius circular features.

B. Surfactant-assisted modulation of roughness

To evaluate surfactant-assisted BOE etching, Triton X-100 was selectively introduced into the BOE etchant at 0 °C for 2 hours, as summarized in Table 1 (samples #3 and #5). A concentration of approximately 0.01 vol% was employed, which is sufficient to induce measurable interfacial effects without altering the bulk etching chemistry.

Triton X-100 is a non-ionic surfactant that lowers interfacial energy and surface tension in aqueous solutions.[33,34] During wet etching of SiO_2, etching pits are primarily associated with spatially non-uniform mass transport at the solid–liquid interface. One key origin of such non-uniformity is the attachment of microbubbles formed from dissolved gases, which preferentially accumulate along sidewalls and at corner regions. These bubbles locally block direct contact between the etchant and the surface, while simultaneously creating regions of enhanced mass transport along their periphery due to bypass flow and concentration gradients.[35,36] This combination of locally suppressed and locally enhanced etching leads to spatial variations in the etch rate, giving rise to differential material removal and ultimately resulting in pit formation.

The addition of Triton X-100 mitigates this effect by reducing surface tension, thereby promoting bubble detachment and preventing their stable attachment on the surface.[37,38] In addition, improved wettability enhances the uniform spreading of the etchant, leading to a more homogeneous solid–liquid interface. As a result, local mass-transport heterogeneity is reduced, suppressing the formation of etching pits.

As shown in Fig. 3, sample #3 exhibits a relatively high areal density of etching pits (approximately 7×10^{-3} μm^{-2}) dis-

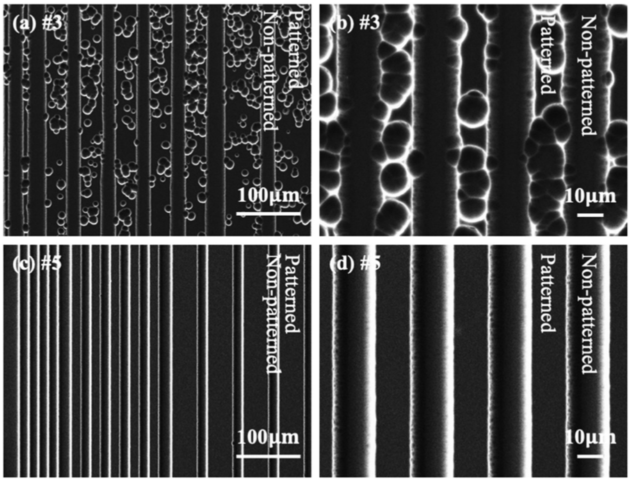

Fig. 3 Top SEM view of the samples comparison of etch spots in BOE under identical conditions (0 °C, 2 h, HF : NH_4F = 1 : 6). (a) No Triton X-100 addition, 25, 50, 75 μm-wide stripes; (b) no Triton X-100 addition, 25 μm-wide stripes; (c) with 0.3 mL Triton X-100 addition, 10, 25, 50 μm-wide stripes; (d) with 0.3 mL Triton X-100 addition, 25 μm-wide stripes.

tributed along the patterned stripes, whereas sample #5 reveals a huge reduction in pit density together with a substantially more uniform etching profile. These observations indicate that introducing Triton X-100 as a surfactant effectively improves sidewall contour continuity and suppresses etching pit formation during BOE-based SiO_2 etching. Overall, Triton X-100 serves as an effective process modifier, enabling finer etching with a markedly reduced density of etching pits and ultimately enhancing the overall etch-profile quality.

C. Effect of reduced temperature on directional etching

To isolate the influence of temperature on wet etching, comparative experiments were conducted at 0 °C and 25 °C under otherwise identical conditions, using BOE with 0.3 mL Triton X-100. A fixed etching duration of 2 h was adopted for consistency across samples, as summarized in Table 1 (samples #4 and #5). As BOE etches Cr approximately three orders of magnitude more slowly than SiO_2, a 40 nm thick Cr mask was sufficient. The cross-sectional SEM image in Fig. S1 further confirms intimate adhesion at the Cr/SiO_2 interface. A fixed etching time of 2 hours was employed throughout to ensure experimental consistency and enable reliable comparison while maintaining intact patterned features after etching. Importantly, this duration was selected to preserve patterned features of varying dimensions, avoiding excessive lateral etching that could otherwise lead to pattern degradation or detachment.

Although BOE etching of SiO_2 is conventionally regarded as isotropic,[27,28] temperature modulation enables controllable near-anisotropy. The etch profile evolution can be decomposed into vertical etching of the exposed SiO_2 surface and lateral propagating beneath the mask opening.[6] Owing to the confined under-mask geometry, lateral etching is more sensitive to variations in reaction kinetics and mass transport than vertical etching.[39] At reduced etching temperature, reaction pathways associated with higher effective kinetic barriers, such as those governing under-mask lateral etching, are preferentially suppressed.[39] Simultaneously, increased solution viscosity weakens diffusion within the confined lateral channel, where reactant replenishment is diffusion-limited.[40,41] The combined effects selectively reduce lateral etching while minimally affecting vertical etching, thereby enhancing etch anisotropy. A more detailed mechanistic analysis is provided in the SI.

This transition is evident in Fig. 4 and is quantified in Table 2, where lateral and vertical etch rates, the vertical-to-lateral etch-rate ratio, and α were averaged over at least 20 measurement locations for each condition. SEM cross-section images from six representative measurement locations for the etching conditions of Table 1 (samples #2, #4, and #5) are presented in Fig. S2–S4, with the corresponding mean values and standard deviations summarized in Tables S1–S3. Quantitative comparison between samples #2 and #4 indicates that the addition of Triton X-100 does not measurably alter the degree of etch anisotropy at 25 °C. By contrast, comparison between samples #4 and #5 demonstrates a pronounced temperature effect. When the etching temperature is reduced to 0 °C, the profiles develop steeper, near-linear sidewalls and a smaller inclination angle of $\alpha = 14.97° \pm 0.40°$, corresponding to a reduction of 7.35° (32.9%). This change is accompanied by an increase in the vertical-to-lateral etch-rate ratio from 1.15 to 1.33, indicating effective suppression of lateral undercut. Overall, reducing the etching temperature decreases the relative contribution of lateral etching with respect to vertical etching. This effect improves sidewall linearity and provides a straightforward handle for enhanced engineering near-anisotropy and profile fidelity in BOE-based SiO_2 wet etching.

Notably, benchmarking against representative wet-etching studies in Fig. 5 reveals that this work achieves one of the

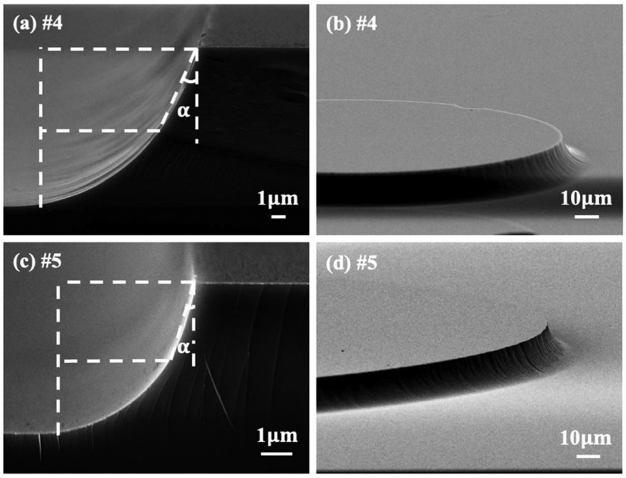

Fig. 4 SEM images of etch profiles under identical conditions (HF : NH_4F = 1 : 6, 0.3 mL of Triton X-100, 2 h). (a) 25 °C, 25 μm-wide stripes; (b) 25 °C, 100 μm-radius circular features; (c) 0 °C, 25 μm-wide stripes; (d) 0 °C, 100 μm-radius circular features.

Table 2 Measured lateral and vertical etching rates, vertical-to-lateral ratio, and etch angle (α)

Sample number #	Lateral etching rate (μm h^{-1})	Vertical etching rate (μm h^{-1})	Ratio (vertical/lateral)	Etch angle α (deg)
1	—	—	—	—
2	5.12 ± 0.03	5.76 ± 0.03	1.13	21.79 ± 0.71
3	—	—	—	—
4	4.52 ± 0.04	5.29 ± 0.01	1.17	22.84 ± 0.42
5	1.84 ± 0.02	2.45 ± 0.01	1.33	14.97 ± 0.40

α is defined as the angle between the vertical axis and the line from the mask edge to the etched profile at half the etch depth.

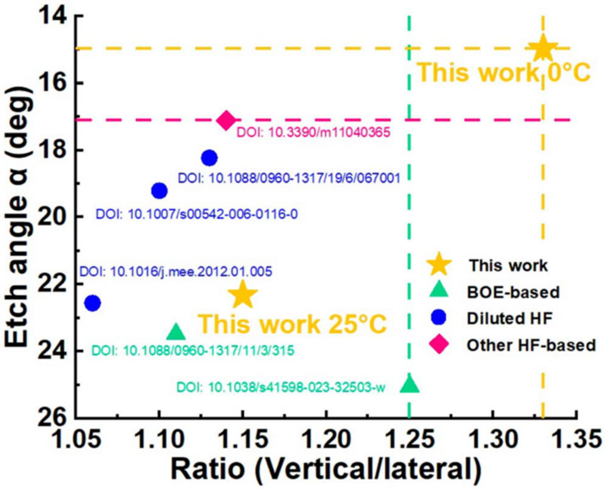

Fig. 5 Comparison of this work with representative state-of-the-art BOE-based wet-etching studies. Note that lower etch angles and higher vertical-to-lateral etch-rate ratios indicate improved performance.

lowest reported etch angles while maintaining a broad and tunable anisotropy window. This result highlights the practical viability of the proposed strategy or controllable sidewall engineering in wet etching. The combination of tunability, process simplicity, and scalability further positions this approach as a promising route for SiO_2 microfabrication with engineered sidewall profiles and suggests its applicability to devices such as waveguides, surface-relief grating couplers, and other diffractive optical elements.

IV. Summary and conclusion

In conclusion, this work establishes a BOE-based wet-etching strategy that enables controllable anisotropic patterning of SiO_2 using a fully wet-chemical process, without recourse to complex or high-cost fabrication platforms. By combining buffered fluoride chemistry for etch-rate stability, surfactant-assisted wetting to suppress local etch non-uniformity, and temperature modulation to preferentially attenuate lateral etching, the traditionally isotropic nature of HF-based wet etching is effectively overcome.

Under optimized conditions, a pronounced improvement in anisotropic sidewall profile and surface integrity is achieved, corresponding to a ~33% reduction in the sidewall angle together with a 16% increase in the vertical-to-lateral etch-rate ratio. These results demonstrate a substantial enhancement in anisotropic selectivity while maintaining etch rates compatible with practical microfabrication workflows. Beyond the specific parameter space explored here, the proposed strategy provides a robust and tunable process window for engineering SiO_2 sidewall geometries with high reproducibility and scalability.

From an application perspective, the ability to realize near-anisotropic, low-roughness SiO_2 microstructures using a scalable wet-etching approach is directly relevant to the fabrication of surface-relief gratings, integrated waveguides, and grating couplers. More broadly, such geometry-controlled dielectric structures form a critical technological foundation for diffractive metasurfaces, free-space optical interconnects, and emerging photonic computing architectures, including optical neural networks and hardware-level artificial intelligence. Against this background, the present work provides a practical materials-processing pathway that supports the manufacturability and large-area deployment of precision SiO_2 photonic structures required for next-generation optical information processing systems.

Author contributions

J. S. and A. P. contributed equally to this manuscript. J. S. and A. P. conceived the main idea, collected and analyzed the data, and wrote the manuscript. D. B supervised the project, provided critical feedback, and revised the manuscript. All other authors discussed the results, edited, and approved the manuscript.

Conflicts of interest

The authors declare that they have no known competing financial interests or personal relationships that could have appeared to influence the work reported in this paper.

Data availability

The authors confirm that all data supporting the findings of this study are available within the article and its supplementary information (SI). Supplementary information is available.

The Supplementary Information quantifies SiO_2 wet-etch anisotropy and provides supporting data for the temperature-dependent suppression of lateral etching. See DOI: https://doi.org/10.1039/d6nr01509c.

Acknowledgements

This work was carried out using the nanofabrication facilities at the Quantum-Nano Fabrication and Characterization Facility (QNFCF), which is funded by the Canada Foundation for Innovation (CFI), the Ontario Ministry of Research, Innovation and Science. This research was also supported by the Natural Sciences and Engineering Research Council of Canada (NSERC). No artificial intelligence tools were used in the experimental design, data acquisition, or data analysis in this work.

References

1 A. U. Sapre, J. Vlček, E. de Prado, L. Fekete, M. Klementová, M. Vondráček, P. Svora, E. Cuza, G. G. Morgan, J. Honolka and I. A. Kühne, Investigating the thin film growth of [Ni(Hvanox)_2] by microscopic and spectroscopic techniques, *Nanoscale Adv.*, 2025, **7**, 2083–2091.

2 F. Kotz, P. Risch, K. Arnold, S. Sevim, J. Puigmartí-Luis, A. Quick, M. Thiel, A. Hrynevich, P. D. Dalton, D. Helmer and B. E. Rapp, Fabrication of arbitrary three-dimensional suspended hollow microstructures in transparent fused silica glass, *Nat. Commun.*, 2019, **10**, 1439.

3 L. A. Moore and C. M. Smith, Fused silica as an optical material, *Opt. Mater. Express*, 2022, **12**, 3043–3059.

4 K. Choi, S.-W. Kim, J.-H. Lee, B. Chu and D.-Y. Jeong, Eco-friendly glass wet etching for MEMS application: A review, *J. Am. Ceram. Soc.*, 2024, **107**, 6497–6515.

5 Z. Li, Y. Jia, K. Duan, R. Xiao, J. Qiao, S. Liang, S. Wang, J. Chen, H. Wu, Y. Lu and X. Wen, One-photon three-dimensional printed fused silica glass with sub-micron features, *Nat. Commun.*, 2024, **15**, 2689.

6 V. Sahu, P. Dewangan, R. V. Vardhan, V. Rinfela, P. K. Menon and P. Pal, A study on chromium thin film with positive photoresist as a masking layer towards the wet bulk micromachining of Borofloat glass, *Micro Nano Syst. Lett.*, 2024, **12**, 12.

7 Y. Dong, *et al.*, Etching of quartz crystals in liquid phase environment: A review, *Nanotechnol. Precis. Eng.*, 2024, **7**, 025001.

8 H. Rai, K. R. Singh, S. S. Pandey and A. Natarajan, Role of Si and SiO_2 in optoelectronic device fabrication, *J. Mol. Struct.*, 2024, **1316**, 138994.

9 B. Hermann, O. Bernard, L. Muscarella and Y. Bellouard, High-efficiency non-ablative UV laser nano-scale processing of fused silica by stable filamentation, *Opt. Express*, 2023, **31**, 29085.

10 Q. Chen, S. Wu, L. Zhang, H. Zhou, W. Fan and C. S. Tan, Transferable single-layer GeSn nanomembrane resonant-cavity-enhanced photodetectors for 2 μm band optical communication and multi-spectral short-wave infrared sensing, *Nanoscale*, 2022, **14**, 7341–7349.

11 Y. Chen, X. Sun, L. Tan, Y. Jiang, Y. Zhou, W. Zhang and G. Zhai, All-optical synthesis chip for large-scale intelligent semantic vision generation, *Science*, 2025, **390**, 1259–1265.

12 J. Hu, D. Mengu, D. C. Tzarouchis, B. Edwards, N. Engheta and A. Ozcan, Diffractive optical computing in free space, *Nat. Commun.*, 2024, **15**, 1525.

13 M. Belt, M. L. Davenport, J. E. Bowers and D. J. Blumenthal, Ultra-low-loss Ta_2O_5-core/SiO_2-clad planar waveguides on Si substrates, *Optica*, 2017, **4**, 532–536.

14 Y. Ding, *et al.*, Waveguide-based augmented reality displays: perspectives and challenges, *eLight*, 2023, **3**, 24.

15 K. Höflich, *et al.*, Roadmap for focused ion beam technologies, *Appl. Phys. Rev.*, 2023, **10**, 041311.

16 A. V. Rumyantsev, N. I. Borgardt, R. L. Volkov and Y. A. Chaplygin, Study of silicon dioxide focused ion beam sputtering using electron microscopy imaging and level set simulation, *Vacuum*, 2022, **202**, 111128.

17 D. A. M. de Winter and J. J. L. Mulders, Redeposition characteristics of focused ion beam milling for nanofabrication, *J. Vac. Sci. Technol., B:Microelectron. Nanometer Struct.–Process., Meas., Phenom.*, 2007, **25**, 2215–2218.

18 A. C. Madison, J. S. Villarrubia, K.-T. Liao, C. R. Copeland, J. Schumacher, K. Siebein, B. R. Ilic, J. A. Liddle and S. M. Stavis, Unmasking the resolution–throughput tradespace of focused-ion-beam machining, *Adv. Funct. Mater.*, 2022, **32**, 2111840.

19 K. Karimi, A. Fardoost, N. Mhatre, J. Rajan, D. Boisvert and M. Javanmard, A thorough review of emerging technologies in micro- and nanochannel fabrication: limitations, applications, and comparison, *Micromachines*, 2024, **15**, 1274.

20 B. X. E. Desbiolles, A. Bertsch and P. Renaud, Ion beam etching redeposition for 3D multimaterial nanostructure manufacturing, *Microsyst. Nanoeng.*, 2019, **5**, 11.

21 A. Pan, C. Zhu, Z. Yan, X. Zhu, Z. Liu and B. Cui, Fabrication of the highly ordered silicon nanocone array with sub-5 nm tip apex by tapered silicon oxide mask, *IEEE Trans. Semicond. Manuf.*, 2024, **37**, 160–165.

22 C. Weigel, *et al.*, Perspectives of reactive ion etching of silicate glasses for optical microsystems, *J. Opt. Microsyst.*, 2021, **1**, 040901.

23 B. Erbas, A. Conde-Rubio, X. Liu, J. Pernollet, Z. Wang, A. Bertsch, M. Penedo, G. Fantner, M. Banerjee, A. Kis, G. Boero and J. Brugger, Combining thermal scanning probe lithography and dry etching for grayscale nanopattern amplification, *Microsyst. Nanoeng.*, 2024, **10**, 28.

24 M. Huff, Recent advances in reactive ion etching and applications of high-aspect-ratio microfabrication, *Micromachines*, 2021, **12**, 991.

25 A. Pan, X. Zhu, C. Zhu, J. Yin, M. S. Hasan, Z. Liu, D. Ban and B. Cui, Batch fabrication of ultra-sharp atomic force microscope probes with stair-shaped handles for high-precision imaging, *Microsyst. Nanoeng.*, 2025, **11**, 188.

26 R. V. Vardhan, V. Sahu, P. Dewangan, Y. K. Srivastava and P. Pal, A comprehensive review on the fabrication of glass microstructures via wet bulk micromachining in HF-based etchants with different masks, *Int. J. Appl. Glass Sci.*, 2025, **396**, 117194.

27 T. G. Konstantinova, *et al.*, Deep multilevel wet etching of fused silica glass microstructures in BOE solution, *Sci. Rep.*, 2023, **13**, 5228.

28 Shubhava, A. Jayarama, G. K. Kannarpady, S. Kale, S. Prabhu and R. Pinto, Chemical etching of glasses in hydrofluoric acid: a brief review, *Mater. Today: Proc.*, 2022, **55**, 46–51.

29 R. Kirchner, *et al.*, Anisotropic etching of pyramidal silica reliefs with metal masks and hydrofluoric acid, *Small*, 2020, **16**, 2002290.

30 B. Kim, W. Lee and S. Lim, Understanding the contributions of F^-, HF, and HF_2^- to the etching of SiO_2 and unveiling the reaction kinetics to represent etching behavior of SiO_2 up to pH 5, *Appl. Surf. Sci.*, 2024, **657**, 159829.

31 Y. Wan, X. Luan, L. Zhou and F. Wu, Wet etching of quartz using a solution based on organic solvents and anhydrous hydrofluoric acid, *Materials*, 2022, **15**, 6475.

32 D. M. Knotter, Etching mechanism of vitreous silicon dioxide in HF-based solutions, *J. Am. Chem. Soc.*, 2000, **122**, 4345–4351.

33 S. M. B. Dissanayake, *et al.*, Effect of Triton X-100 surfactant concentration on the wettability of polyethylene-based separators used in supercapacitors, *J. Sci.:Adv. Mater. Devices*, 2024, **9**, 100801.

34 Aisha, *et al.*, Wetting the surface: a deep dive into chemistry and applications of surfactants, *Clean Chem Eng.*, 2025, **11**, 100197.

35 M. Yao, B. Tang, K. Sato and W. Su, Silicon anisotropic etching in Triton-mixed and isopropyl alcohol-mixed tetramethyl ammonium hydroxide solution, *Micro Nano Lett.*, 2015, **10**, 469–471.

36 H. S. Bindra, J. Ramchandran and R. Nayak, Simplified and cost-effective technique to enhance optical properties of microstructured silicon, *Mater. Today: Proc.*, 2020, **28**, 272–277.

37 D. M. Eckmann and D. P. Cavanagh, Bubble detachment by diffusion-controlled surfactant adsorption, *Colloids Surf., A*, 2003, **227**, 21–33.

38 S. Bhandari, P. Kang, J. Jeong, J. Cao and K. Ehmann, Cavitation bubble removal by surfactants in laser-induced plasma micromachining, *Manuf. Lett.*, 2022, **32**, 96–99.

39 W. M. White, *Geochemistry: chapter 5 kinetics*, 2007, pp. 156–209.

40 Q. Chen, Y. Wang, T. Deng and Z. Liu, Fabrication of nanopores and nanoslits with feature sizes down to 5 nm by wet etching method, *Nanotechnology*, 2018, **29**, 085301.

41 K. R. Williams and R. S. Muller, Etch rates for micromachining processing, *J. Microelectromech. Syst.*, 1996, **5**, 256–269.